

Cite this: DOI: 10.1039/c3cp53642d

www.rsc.org/pccp

PAPER

# Joint Experimental and Computational $^{17}\text{O}$ Solid State NMR Study of Brownmillerite $\text{Ba}_2\text{In}_2\text{O}_5$

Rıza Dervişoğlu,<sup>a,b</sup> Derek S. Middlemiss,<sup>a,b</sup> Frédéric Blanc,<sup>b</sup> Lesley A. Holmes,<sup>a</sup> Yueh-Lin Lee,<sup>c</sup> Dane Morgan,<sup>c</sup> Clare P. Grey<sup>a,b,\*</sup>

Received 28th August 2013, Accepted 2nd December 2013

DOI: 10.1039/c3cp53642d

Structural characterization of Brownmillerite  $\text{Ba}_2\text{In}_2\text{O}_5$  was achieved by an approach combining experimental solid-state NMR spectroscopy, density functional theory (DFT) energetics, and GIPAW NMR calculations. While in the previous study of  $\text{Ba}_2\text{In}_2\text{O}_5$  by Adler *et al.* (S. B. Adler, J. A. Reimer, J. Baltisberger and U. Werner, *J. Am. Chem. Soc.*, 1994, **116**, 675–681), three oxygen resonances were observed in the  $^{17}\text{O}$  NMR spectra and assigned to the three crystallographically unique O sites, the present high resolution  $^{17}\text{O}$  NMR measurements under magic angle spinning (MAS) find only two resonances. The resonances have been assigned using first principles  $^{17}\text{O}$  GIPAW NMR calculations to the combination of the O ions connecting the  $\text{InO}_4$  tetrahedra and the O ions in equatorial sites in octahedral  $\text{InO}_6$  coordination, and to the axial O ions linking the four- and six-fold coordinated  $\text{In}^{3+}$  ions. Possible structural disorder was investigated in two ways: firstly, by inclusion of the high-energy structure also previously studied by Mohn *et al.* (C. E. Mohn, N. L. Allan, C. L. Freeman, P. Ravindran and S. Stølen, *J. Solid State Chem.*, 2005, **178**, 346–355), where the structural O vacancies are stacked rather than staggered as in Brownmillerite and, secondly, by exploring structures derived from the ground-state structure but with randomly perturbed atomic positions. There is no noticeable NMR evidence for any substantial occupancy of the high-energy structure at room temperature.

## 1. Introduction

Perovskites are a broad class of materials that find widespread application, notably here as electrolytes for intermediate temperature fuel cells as a consequence of their high oxygen and, when hydrated, their even higher proton conductivities.<sup>1</sup> They are increasingly recognized as competitors to more conventional electrolyte phases such as yttria-stabilized zirconia (YSZ) and other fluorite-structured compounds. The structural family possesses the  $\text{ABO}_3$  stoichiometry where the A-cations are typically rare-earth or alkaline-earth metals; and the B-cations, transition metals or semi-metals<sup>2</sup> of varying oxidation states and ionic radii. The B-site cations are each bonded to six O ions to form corner-sharing  $\text{BO}_6$  octahedra, while the A-site cations occupy the cubic space delimited by eight  $\text{BO}_6$  units, and in turn coordinate with twelve nearest-neighboring O ions. Anisotropic expansion of the unit cell and significant tilting of the octahedra may occur as a function of relative size of the cations. The tuning of such distortions may lead to increased ionic conductivity due to change of total lattice energies, or more specifically, to variations in the diffusion bottlenecks of a given structure.<sup>3</sup> The ideal perovskite structure manifests a simple cubic cell with space group  $Pm\bar{3}m$ . Doping with lower valent cations typically introduces compensating extrinsic O vacancies, and constitutes

the most frequently pursued strategy to synthesize phases with increased ionic conductivity.

The present study focuses on the  $\text{Ba}_2\text{In}_2\text{O}_5$  defect perovskite phase, a material that, in its high temperature cubic phase (*i.e.*, above 1040°C), displays O ion conductivity significantly exceeding that of YSZ,<sup>4</sup> along with proton conductivity when hydrated.<sup>4–14</sup> Compensation of the  $\text{Ba}^{2+}$  and  $\text{In}^{3+}$  cation charges in  $\text{Ba}_2\text{In}_2\text{O}_5$  requires the removal of one-sixth of the O atoms in the parent perovskite structure, yielding a high intrinsic concentration of O vacancies. The vacancies order at room temperature into an orthorhombic structure with space group  $Ibm2$ .<sup>15,16</sup> Three crystallographically-distinct O sites result, ordered so as to form alternating layers of tetrahedral (Tet, Tet') and octahedral (Oct)  $\text{In}^{3+}$  centered polyhedra, with successive (010) tetrahedral layers offset from one another in an  $\cdots\text{OctTetOctTet}'\cdots$  O vacancy arrangement (Figure 1a, denoted the 'staggered' arrangement). The labeling adopted hereafter places O1 anions at the equatorial positions of the  $\text{InO}_6$  octahedra; O2, bridging octahedra and  $\text{InO}_4$  tetrahedra; and O3, within the tetrahedral layer. The structure is named Brownmillerite after the original  $\text{Ca}_2\text{FeAlO}_5$  mineral, which has a similar arrangement of O vacancies.<sup>15</sup> The  $\text{Ba}_2\text{In}_2\text{O}_5$  structure has been described within a variety of space groups. Gregory and Weller used the  $Ibm2$  space group,<sup>16</sup> and the  $Pnmm$

and *Icmm* space groups have both been suggested based on other Brownmillerite systems.<sup>17,18</sup> The structure shown (Figure 1a) corresponds to the *Ibm2* structure. Fischer *et al.*<sup>19</sup> chose to refine the structure in the *Ima2* space group [corresponding to a different setting of the *Ibm2* group (number 46 from the international tables for crystallography (ITC)<sup>20</sup>)] and derived a structure that is related to the *Ibm2* structure, differing slightly in terms of the In-O bond distances and distortions of the InO<sub>6</sub> octahedra, but in which the octahedral tilting remains unaltered. Speakman *et al.*<sup>17</sup> and Berastegui *et al.*<sup>18</sup>, performed refinements in both the *Ibm2* and *Icmm* space groups, using neutron and X-ray diffraction data. These two space-groups yield more satisfactory fits to the data than any performed using other possible Brownmillerite space groups. They eventually rejected the *Ibm2* structure in favor of an *Icmm* (no. 74 from the ITC<sup>20</sup>) solution on the basis of  $\chi^2/R_w$  values, better fitting of a series of weaker reflections, and more satisfactory site occupancies.<sup>17,18</sup> The resultant structure, is however, disordered, with partial occupancy of In(2) and O3 on the 8i positions. Mohn *et al.*<sup>11</sup> explored these structures by DFT calculations and identified a first high-energy state with an  $\cdots\text{OctTetOctTet}\cdots$  with a stacked O vacancy arrangement (Figure 1b, denoted the 'stacked' arrangement). We calculated a relative energy difference of 5 kJmol<sup>-1</sup> (per Ba<sub>2</sub>In<sub>2</sub>O<sub>5</sub> formula unit) between the ground state and the high-energy structure. Thus, the structural and theoretical studies suggest that the room temperature itself may contain a degree of disorder in regard to both the tilting of octahedra and the oxygen and cation site occupancies, which may be locked in by off equilibrium cooling from high temperature, during synthesis.

Ba<sub>2</sub>In<sub>2</sub>O<sub>5</sub> undergoes a series of phase changes from the room temperature orthorhombic structure just described, to a tetragonal form (space group *I4cm*) above 925 °C, in which O3, O2 and vacant sites exchange.<sup>17</sup> Subsequently a disordered cubic phase forms above approximately 1040-1075 °C.<sup>17,21</sup> It is only in the tetragonal and cubic forms that the material displays substantial ionic conductivity.<sup>4,17</sup> While the presence of a large number of O vacancies in the tetrahedral layers of Ba<sub>2</sub>In<sub>2</sub>O<sub>5</sub> might be thought of as conducive to rapid O conduction, freezing of the vacancies in the low temperature orthorhombic phase allows for only limited O motion.<sup>4</sup> Hydration of Ba<sub>2</sub>In<sub>2</sub>O<sub>5</sub> at moderate temperatures results in a tetragonal structure with space group *P4/mbm* within which the intrinsic O3 layer vacancies of Ba<sub>2</sub>In<sub>2</sub>O<sub>5</sub> are fully occupied by the O atoms of water, as described by Jayaraman *et al.*<sup>5</sup>

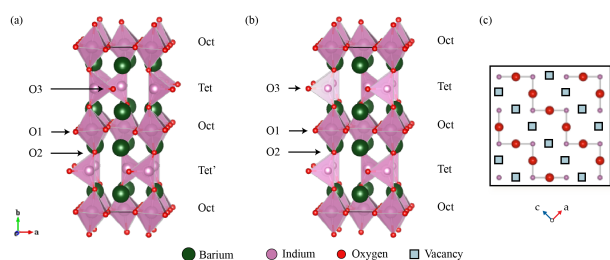


**Figure 1.** Room temperature crystal structure of (a) ground state orthorhombic Brownmillerite Ba<sub>2</sub>In<sub>2</sub>O<sub>5</sub> in space group *Ibm2* with  $\cdots\text{OctTetOctTet}\cdots$  staggered O vacancy arrangement and (b) the higher energy  $\cdots\text{OctTetOctTet}\cdots$  stacked O vacancy arrangement.<sup>15,16</sup> (c) Schematic representation of the O3 layer showing the O vacancy ordering.

Previous solid-state <sup>17</sup>O NMR measurements under static, magic angle spinning (MAS) and dynamic angle spinning (DAS)<sup>22</sup> by Adler *et al.*<sup>7</sup> observed three <sup>17</sup>O resonances at room temperature: two very broad peaks that were attributed to the O1 and O2 environments, and a narrow peak at 220 ppm assigned to the O3 environment. The peak broadening and line shapes of the O1 and O2 environments were ascribed to second-order quadrupolar effects arising out of the highly asymmetric distributions of charge at these sites.<sup>2</sup> The narrow third resonance was shown to nutate rapidly (on the order of liquid H<sub>2</sub><sup>17</sup>O), and was attributed to a site lying upon a crystallographic inversion center (in space group *Pcmm*, as used in the earlier structural refinements).<sup>23</sup> However, as discussed above, Speakman *et al.*<sup>17</sup> subsequently showed that Ba<sub>2</sub>In<sub>2</sub>O<sub>5</sub> crystallizes in an orthorhombic structure with space group *Ibm2* or *Icmm* rather than *Pcmm*, both space groups lacking oxygen sites on an inversion center, suggesting that the previous assignment by Adler *et al.*<sup>7</sup> of the <sup>17</sup>O NMR spectra of Ba<sub>2</sub>In<sub>2</sub>O<sub>5</sub> was based on an inaccurate crystallographic model. Furthermore, the presence or lack of inversion symmetry does not necessarily imply a non-zero quadrupole coupling constant, C<sub>Q</sub>, so the origin and assignment of this third resonance remains unclear.

Brownmillerite Ba<sub>2</sub>In<sub>2</sub>O<sub>5</sub> has also been the subject of a number of prior theoretical studies, largely focused on understanding the O transport mechanisms, phase transformations and the structure of the hydrated phase.<sup>8,11,24-27</sup> Of particular relevance to the present work, Mohn *et al.* performed a comprehensive treatment of the energy hypersurface of a 36-atom supercell of Ba<sub>2</sub>In<sub>2</sub>O<sub>5</sub> within a series of periodic density functional theory (DFT) calculations and showed that the orthorhombic structure with staggered O vacancy arrangement (Figure 1a) is favored over the stacked arrangement (Figure 1b) as discussed earlier,<sup>11,28</sup> and in agreement with experimental findings by Gregory and Weller<sup>16</sup>. Optimizations of all crystallographically inequivalent configurations in a reasonable supercell provided static thermodynamic parameters directly, revealing in particular that the low energy minima all conserve the 50% tetrahedral to 50% octahedral InO<sub>n</sub> alternating layer motif (where “n” is the coordination number). More recently, Lee *et al.*<sup>29</sup> used DFT energies to parameterize a cluster expansion of the O-Va (Va=vacancy) pseudo-binary system. They predicted a complete phase diagram associated with O-Va ordering in good qualitative agreement with experiments, including the Brownmillerite ground state at low-temperature, while upon heating they predicted first the onset of a partially disordered tetragonal phase by a first-order transition and the subsequent formation of a fully disordered cubic phase by a second-order transition.

The current work re-examines Ba<sub>2</sub>In<sub>2</sub>O<sub>5</sub> using contemporary solid state <sup>17</sup>O NMR spectroscopy techniques, applying higher field strengths than previous studies and two-dimensional multiple-quantum magic angle spinning (MQMAS) experiments.<sup>30,31</sup> A technique that had not been developed when the previous <sup>17</sup>O NMR study of Ba<sub>2</sub>In<sub>2</sub>O<sub>5</sub> was reported by Adler *et al.*<sup>7</sup> and which allows high-resolution solid state NMR spectra of quadrupolar nuclei (such as <sup>17</sup>O, spin I = 5/2) to be obtained. The application of a similar approach to the hydrated Ba<sub>2</sub>In<sub>2</sub>O<sub>5</sub> [*i.e.* Ba<sub>2</sub>In<sub>2</sub>O<sub>4</sub>(OH)<sub>2</sub>] phase will be presented in a subsequent paper.<sup>32</sup> First principles periodic DFT NMR calculations within the gauge-including projector augmented wave (GIPAW)

approach<sup>33</sup> are also performed, providing a robust interpretation of the experimental spectral assignments. Similar theoretical approaches have previously been fruitfully applied to a very large range of systems.<sup>34–37</sup> Relevant studies of related phases including the <sup>17</sup>O and <sup>29</sup>Si spectra of the MgSiO<sub>3</sub> perovskite,<sup>38</sup> the multinuclear <sup>23</sup>Na and <sup>93</sup>Nb MQMAS spectra of the NaNbO<sub>3</sub> and NaTaO<sub>3</sub> perovskites<sup>39,41</sup> by Ashbrook *et al.*, and some of the current authors' recent work on pure and doped LaGaO<sub>3</sub><sup>42,43</sup> and BaSnO<sub>3</sub><sup>44</sup> perovskites. We first present the DFT calculations of Ba<sub>2</sub>In<sub>2</sub>O<sub>5</sub>, examining a series of energetically similar structures. The energetics calculations are then used in combination with the GIPAW NMR data to help assign the experimental <sup>17</sup>O NMR data to the specific O environments in Ba<sub>2</sub>In<sub>2</sub>O<sub>5</sub>.

## 2. Materials and Methods

### 2.1. Experimental section

#### 2.1.1. Sample preparation

Ba<sub>2</sub>In<sub>2</sub>O<sub>5</sub> powder was prepared by a solid state route<sup>45</sup> using stoichiometric quantities of BaCO<sub>3</sub> (Sigma-Aldrich, ≥ 99%) and In<sub>2</sub>O<sub>3</sub> (Sigma-Aldrich, 99.99% trace metals basis) which were first ground in a planetary ball mill (Retsch PM100) at 600 rpm for 4 h. The powder was then pelletized, sintered at 1300 °C for 24 h and re-ground by mortar and pestle, and these steps were repeated until a pure phase was obtained as determined by powder X-ray diffraction (Figure S1). <sup>17</sup>O enriched Ba<sub>2</sub>In<sub>2</sub>O<sub>5</sub> was obtained by heating dry Ba<sub>2</sub>In<sub>2</sub>O<sub>5</sub> (dried at 900 °C under vacuum for 12 h) in 50% <sup>17</sup>O enriched O<sub>2</sub> gas (Isotec, 99%, used as received) in a sealed quartz tube at 1000 °C for 24 h.<sup>46</sup> Powder X-ray diffraction patterns were obtained on Panalytical Empyrean and Bruker D8-Focus X-ray diffractometers using Cu K<sub>α</sub> radiation (λ = 1.5418 Å) (Figure S1 in the Supplementary Information).

#### 2.1.2. Solid State NMR Spectroscopy

Solid state <sup>17</sup>O MAS NMR experiments on <sup>17</sup>O enriched Ba<sub>2</sub>In<sub>2</sub>O<sub>5</sub> were performed on a 9.4 T Bruker Avance 400 MHz spectrometer using a Bruker 4 mm HX probe; a 11.7 T Oxford magnet with a Varian Infinity Plus 500 MHz spectrometer using a Chemagnetics 4mm HX probe; a 14.1 T Bruker Avance 600 MHz spectrometer using a Bruker 4 mm HFX probe; and finally, a 21.1 T Bruker Avance II 900 MHz spectrometer equipped with a 3.2 mm HX probe. Spectra were recorded using a  $\sim\pi/2$  pulse length of 1.2 μs at a radio frequency (RF) field amplitude of  $\sim 70$  kHz and a MAS frequency of 15 kHz at 9.4, 11.7, 14.1 T, and a  $\sim\pi/2$  pulse length of  $\sim 2$  μs at a RF field amplitude of  $\sim 40$  kHz and a MAS frequency of 20 kHz at 21.1 T. The <sup>17</sup>O two dimensional (2D) triple-quantum MAS (3QMAS)<sup>30,31,47</sup> experiments (using a z-filter<sup>30,31,47</sup> pulse sequence) of <sup>17</sup>O enriched Ba<sub>2</sub>In<sub>2</sub>O<sub>5</sub> were carried out at 14.1 T and at a MAS frequency of 13 kHz. Twenty-eight t<sub>1</sub> increments of 1024 scans were co-added. Hard and soft pulses were performed at RF fields of  $\sim 80$  and  $\sim 10$  kHz, respectively. All <sup>17</sup>O NMR data were collected on freshly <sup>17</sup>O enriched samples packed in ZrO<sub>2</sub> rotors. A recycle delay of 10 s was used for all experiments averaging  $\sim 6500$  to  $\sim 30000$  scans. <sup>17</sup>O chemical shifts were externally referenced to water at 0.0 ppm at 20 °C. NMR data were processed using Bruker TopSpin 3.0<sup>48</sup>, and the MatNMR<sup>49</sup> packages, the latter running on MatLab. Simulations and deconvolutions were also performed using the

same software packages.

### 2.2. Computational Methods

#### 2.2.1. Energetics and configurations

The first principles solid-state electronic structure calculations used here are similar to those used in various recent studies of oxides and gallates,<sup>50</sup> perovskites<sup>41,42,44,51</sup> and pyrochlores,<sup>52,53</sup> and were all performed within the projector augmented wave approach in the CASTEP code.<sup>54</sup> Full structural optimizations (both cell and atomic positions) of Ba<sub>2</sub>In<sub>2</sub>O<sub>5</sub> were performed in the absence of any symmetry constraints (*i.e.* space group P1), a plane wave kinetic energy cut-off of 40 Ry and a linear spacing of 0.04 Å<sup>-1</sup> or smaller for the reciprocal space sampling mesh, yielding Monkhorst-Pack meshes of dimension 5×2×5 for the Ba<sub>8</sub>In<sub>8</sub>O<sub>20</sub> supercell. NMR is very sensitive to small deviations in atomic positions, and so we have averaged NMR parameters over multiple fully relaxed structures starting from similar but slightly different, randomly perturbed atomic positions. This process yields insight into the sensitivity of the computed NMR parameters to the small variations in bond lengths and angles arising out of the finite numerical accuracy of the simulations.

All the geometry parameters (Table 1) reported subsequently were averaged over five  $\cdots\text{OctTetOctTet}\cdots$  (Figure 1a) and four  $\cdots\text{OctTetOctTet}\cdots$  (Figure 1b) Ba<sub>2</sub>In<sub>2</sub>O<sub>5</sub> DFT optimized configurations, proceeding from initial configurations in which the unit cell sizes and atomic positions were randomly perturbed over a 0.0 to 0.1 Å length scale. The resultant optimized configurations for both  $\cdots\text{OctTetOctTet}\cdots$  and  $\cdots\text{OctTetOctTet}\cdots$  differ in energy by 0.2 kJmol<sup>-1</sup> (per formula unit) within each set and by 5.0 kJmol<sup>-1</sup> (per formula unit) between sets, where the  $\cdots\text{OctTetOctTet}\cdots$  configurations all lie lower in energy. The octahedral and tetrahedral tilts are all the same within given sets. All of these structures are detailed in the Supplementary Information (SI). The Perdew-Burke-Ernzerhof GGA-type exchange-correlation functional has been used throughout.<sup>55</sup> Convergence of total energy with respect to numerical parameters was estimated at 0.2 kJmol<sup>-1</sup> per atom or better. Optimisations were pursued until energy difference, maximum atomic force, maximum atomic displacement and maximum stress tensor component fell below tolerances of 1×10<sup>-6</sup> eV, 1×10<sup>-3</sup> eVÅ<sup>-1</sup>, 1×10<sup>-3</sup> Å and 5×10<sup>-3</sup> GPa, respectively. The effect of decreasing the tolerances listed above by a further order of magnitude was investigated, yielding only minimal changes in geometry and computed NMR parameters. Oxygen ion Mulliken charges and O-In bond population overlaps were also calculated.<sup>56,57</sup>

#### 2.2.2. NMR Calculations

Fully periodic calculations of NMR parameters within the gauge-including projector augmented wave (GIPAW) method<sup>33,58</sup> have also been performed within the CASTEP code,<sup>54</sup> including determinations of the electric field gradient tensors and associated quadrupolar interaction parameters for <sup>17</sup>O sites.<sup>59</sup> The NMR parameters were obtained by a single point calculation within each optimised geometry, differing only from the earlier optimizations in that a larger basis set cut-off of 60 Ry was applied. The isotropic shielding was obtained as  $\sigma_{\text{iso}} = \frac{1}{3}(\sigma_{\text{xx}} + \sigma_{\text{yy}} + \sigma_{\text{zz}})$ , where  $\sigma_{\text{xx}}$ ,  $\sigma_{\text{yy}}$  and  $\sigma_{\text{zz}}$  are the principal components of the shielding tensor, ordered such that  $|\sigma_{\text{zz}} - \sigma_{\text{iso}}| \geq |\sigma_{\text{xx}} - \sigma_{\text{iso}}| \geq$

$|\sigma_{yy} - \sigma_{iso}|$ . The isotropic chemical shift  $\delta_{iso}$  is then derived from the computed site shielding  $\sigma_{iso}$  by application of a shielding reference  $\sigma_{ref}$  according to  $\delta_{iso} = \sigma_{ref} + m\sigma_{iso}$ . Both  $\sigma_{ref}$  and  $m$  for  $^{17}\text{O}$  are obtained from the previous work of some of the current authors which yielded  $\sigma_{ref} = 223.70 \pm 3.03$  ppm,  $m = -0.888 \pm 0.014$  with a mean absolute error (MAE) in computed  $\delta_{iso}$  values of 12.1 ppm relative to experiment.<sup>50</sup> The chemical shift anisotropy and asymmetry are also computed, defined as  $\delta_{aniso} = \sigma_{zz} - \frac{1}{2}(\sigma_{xx} + \sigma_{yy})$  and  $\eta_{cs} = (\sigma_{yy} - \sigma_{xx})/(\sigma_{zz} - \sigma_{iso})$ , respectively. The quadrupole coupling constant for  $^{17}\text{O}$  sites is obtained as  $C_Q = eQV_{zz}/h$ ; and the asymmetry, as  $\eta_Q = (V_{xx} - V_{yy})/V_{zz}$ ; where an ordering  $|V_{zz}| \geq |V_{yy}| \geq |V_{xx}|$  of the principal components of the traceless electric field gradient tensor is assumed. An experimental value  $Q = -0.02558$  barns has been used for the  $^{17}\text{O}$  nuclear electric quadrupole moment.<sup>60</sup> All the chemical shift and quadrupolar NMR parameters of  $\text{Ba}_2\text{In}_2\text{O}_5$  were averaged over the five  $\cdots\text{OctTetOctTet}\cdots$  and four  $\cdots\text{OctTetOctTet}\cdots$  optimized configurations obtained starting from perturbed configurations, as discussed above. The full set of computed NMR parameters for each structure are given in the SI. Unless otherwise specified, all the corresponding simulated  $^{17}\text{O}$  NMR spectra were obtained by simulations of single spectra due to each individual O site using the SIMPSON<sup>61</sup> software, and subsequent summation to form the full spectrum for each crystal cell.

### 3. Results and Discussion

#### 3.1 DFT Calculations (Structures and Energetics)

The DFT-based structural optimizations for  $\text{Ba}_2\text{In}_2\text{O}_5$  proceeded from models with *Ibm2* space group proposed by Berastegui *et al.*,<sup>18</sup> Speakman *et al.*<sup>17</sup> and Fischer *et al.*<sup>19</sup> Note that although Speakman *et al.* and Berastegui *et al.* reject the *Ibm2* structure in favour of an *Icmm* solution, it is difficult to reasonably represent a lattice with fractional occupancies in the present theoretical approach, and so we regard the *Ibm2* cell as the closest available structure consistent with the constraint to full site occupancies. The final mean optimized lattice constants, along with relevant mean bond lengths and angles of the *Ibm2* derived  $\cdots\text{OctTetOctTet}\cdots$  arrangement are compared with the ground state *Ibm2* calculated structure of Mohn *et al.*<sup>11</sup>, and the experimental *Ima2* and *Ibm2* structures of Fischer *et al.*<sup>19</sup> and Speakman *et al.*,<sup>17</sup> respectively, in Table 1. The final mean optimised structural parameters deviate markedly from those obtained by Fischer *et al.*,<sup>19</sup> most notably with respect to the internal distortions of the In–O polyhedra away from their respective ideals. Specifically, the optimisation yields  $\text{InO}_6$  octahedra wherein the In–O bond lengths fall in a 4–short and 2–long pattern, in agreement with the *Ibm2* structure of Speakman *et al.*,<sup>17</sup> Berastegui *et al.*,<sup>18</sup> and Gregory and Weller,<sup>16</sup> whereas the Fischer *et al.*<sup>19</sup> structure presents a distortion in the opposite sense. Assuming that the disposition of and standard deviation in the In–O bond lengths makes for a reasonable basis upon which to judge the agreement of the various structures, it is concluded that the present calculations lend more support to the Speakman *et al.* structure.<sup>17</sup> We note again that further tightening of the

optimization tolerances yields no appreciable change in the calculated structural parameters.

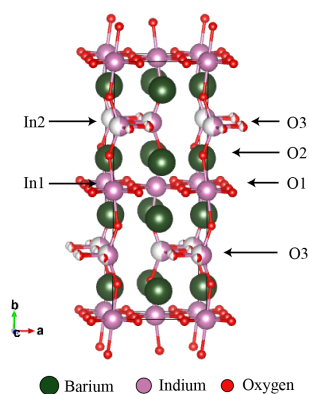


**Figure 2.** (a) The *Icmm* structure proposed by Speakman *et al.*<sup>17</sup> and Berastegui *et al.*<sup>18</sup> illustrating the atomic disorder and partial site occupancy (denoted by sector filling of atoms).

The *Icmm* structure of Speakman *et al.*<sup>17</sup> and Berastegui *et al.*<sup>18</sup> suggests that we need to consider the possibility of residual disorder in the room temperature structure (Figure 2). To explore this, we introduced deviations from the ground state, by randomly perturbing all atomic positions by as much as 0.1 Å as discussed above. After minimization, very few structural differences were observed between these structures (Table 1), their formation energies differing by only 0.2 kJmol<sup>-1</sup> per  $\text{Ba}_2\text{In}_2\text{O}_5$  formula unit. We also investigated the  $\cdots\text{OctTetOctTet}\cdots$  (Figure 1 (b)) high-energy structure of Mohn *et al.*<sup>11</sup> again randomly generating a series of very similar structures. Noticeable variations in In–O–In bond angles of 2–6° are observed between the ground and high-energy structures (Table 1), their energies differing by approximately 5 kJmol<sup>-1</sup> per formula unit.

#### 3.2. Diffraction and NMR

The experimental x-ray powder diffraction patterns obtained here for both  $\text{Ba}_2\text{In}_2\text{O}_5$ <sup>5,16,17</sup> and  $^{17}\text{O}$  enriched  $\text{Ba}_2\text{In}_2\text{O}_5$  are consistent with previous reports<sup>5,17</sup> (Figure S1 in the SI), and indicate that the structures are orthorhombic at room temperature. The patterns match structures modeled in either *Ibm2*<sup>5,16,17</sup> or *Icmm*<sup>17,18</sup> space groups, both yielding very similar diffraction patterns.

The one-dimensional  $^{17}\text{O}$  MAS NMR spectrum of  $^{17}\text{O}$  enriched  $\text{Ba}_2\text{In}_2\text{O}_5$  obtained at 21.1 T shows two similarly broadened and well-resolved resonances centered at 179 and 138 ppm with an intensity ratio of approximately 3:2. An appreciable increase in the broadening of the resonances occurs as the field strength is decreased from 21.1 T to 9.4 T, indicative of the presence of significant second order quadrupolar broadening (Figure 3a). Large quadrupolar coupling constants are to be expected given that the In–O–In environments in the structure are inherently asymmetric, leading to large electric field gradients.

**Table 1.** Cell lengths and angles (Å, °), and In–O bond distances (Å) and In–O–In bond angles (°) involving O1, O2 and O3 sites, as obtained from optimizations of the initial perturbed P1 symmetry Ba<sub>3</sub>In<sub>8</sub>O<sub>20</sub> cells in both the ground ...OctTetOctTet'... (5 structures) and high-energy states ...OctTetOctTet... (4 structures), all compared with corresponding experimental and computational literature values. Means and standard deviations (sd) in the values are shown.

Oxygen Environment		Optimized– Ba <sub>2</sub> In <sub>2</sub> O <sub>5</sub> ground state present calculation (P1) ...OctTetOctTet'...	Optimized– Ba <sub>2</sub> In <sub>2</sub> O <sub>5</sub> high-energy state present calculation (P1) ...OctTetOctTet...	Computational Mohn <i>et al.</i> <sup>11</sup>	Experimental Fischer <i>et al.</i> ( <i>Ima2</i> ) <sup>19</sup>	Experimental Speakman <i>et al.</i> ( <i>Ibm2</i> ) <sup>17</sup>
	(Å, °)	a = 6.233, b = 16.905, c = 6.043 α = 90.0, β = 90.0, γ = 90.0	a = 6.190, b = 17.072, c = 6.045 α = 90.0, β = 90.0, γ = 90.0	a = 6.279, b = 16.841, c = 6.085, α = β = γ = 90	a = 16.719, b = 6.083, c = 5.956, α = β = γ = 90	a = 6.087, b = 16.784, c = 5.970, α = β = γ = 90
In-O1-In	distances (Å)	2.174 (sd 0.000), 2.177 (sd 0.001)	2.160 (sd 0.000), 2.168 (sd 0.001)	2.188, 2.196	1.844, 2.421	2.127, 2.143
	angles (°)	172.2 (sd 0.0)	178.1 (sd 0.3)	-	173.1	173.1
In-O2-In	distances (Å)	2.064 (sd 0.000), 2.364 (sd 0.001)	2.068 (sd 0.001), 2.376 (sd 0.001)	2.096, 2.341	1.927, 2.412	2.012, 2.310
	angles (°)	147.4 (sd 0.1)	150.0 (sd 0.3)	-	149.7	154.6
In-O3-In	distance (Å)	2.111 (sd 0.000), 2.122 (sd 0.000)	2.116 (sd 0.000), 2.125 (sd 0.001)	2.137, 2.144	2.184, 2.369	2.091, 2.109
	angles (°)	127.6 (sd 0.1)	124.6 (sd 0.2)	-	115.8	129.3

As discussed above, structural refinements in space groups *Ibm2* and *Icmm* all give rise to three O sites O1, O2, O3 (Figure 1) occurring in a 2:2:1 ratio. However, only two O chemical environments are detected in the 1D <sup>17</sup>O NMR spectra. Thus, <sup>17</sup>O 3QMAS experiments<sup>30,31,47</sup> were also performed in an effort to try to resolve any additional <sup>17</sup>O sites in Ba<sub>2</sub>In<sub>2</sub>O<sub>5</sub> that may have been missed in the 1D spectra, even at high field. However, again only two <sup>17</sup>O sites in an approximately 3:2 ratio are observed (Figure 3a). Simulations of the <sup>17</sup>O 1D and MQMAS NMR spectra yield a quadrupole coupling constant (*C<sub>Q</sub>*) value of 5.0 (± 0.2) MHz for the O environment associated with the high frequency signal at an isotropic chemical shift  $\delta_{\text{iso}} = 179 \pm 4$  ppm, and a slightly larger value of 5.8 (± 0.2) MHz for the low frequency signal at  $\delta_{\text{iso}} = 138 \pm 4$  ppm in Figures 3 and 4. We note that the high frequency signal shows a slight broadening along the *dy/dx*=+1 direction of the MQMAS spectrum corresponding to a small distribution of chemical shifts,<sup>62,63</sup> suggesting that more than one site might be buried under this resonance. The isotropic shifts obtained from the field dependence of the peak positions in the 1D spectra, (Figure S2; Table 2), differ slightly from those obtained by NMR simulation of the 1D and MQMAS data, suggesting that the data cannot be fit by a single set of NMR parameters for each resonance. The <sup>17</sup>O MAS NMR spectra of the Ba<sub>2</sub>In<sub>2</sub>O<sub>5</sub> presented above are obtained when Ba<sub>2</sub>In<sub>2</sub>O<sub>5</sub> was dried at 1000 °C prior to <sup>17</sup>O enrichment, as discussed above. The resonance at 220 ppm observed previously by Adler *et al.*<sup>7</sup> appears only very weakly in the 8.5 T spectrum in Figure 3, and its presence depends strongly on the  $\pi/2$  pulse length used to acquire the spectra. It cannot reasonably be ascribed to a BaO impurity, which might be present if the sintering step of the Ba<sub>2</sub>In<sub>2</sub>O<sub>5</sub> synthesis was not complete, since this would give rise to a much higher shift at  $\delta_{\text{iso}} = 629$  ppm.<sup>64</sup> The most likely assignment of this resonance is that it is due to surface water. Having identified water as a potential source of this resonance following the measurement performed at 8.5 T, the samples were kept in a desiccator, helping to minimize the intensity of this resonance in subsequent experiments.

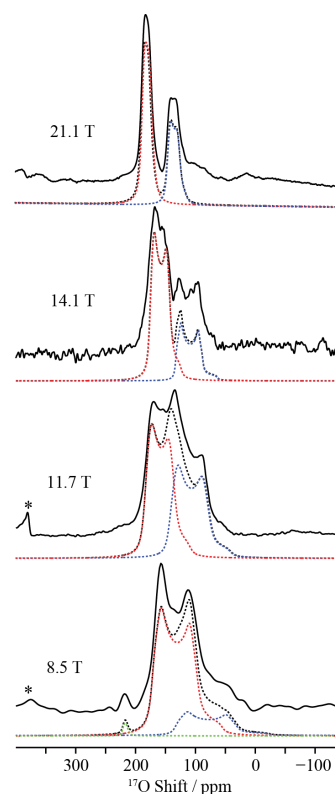


**Figure 3.** <sup>17</sup>O MAS NMR spectra of <sup>17</sup>O enriched Ba<sub>2</sub>In<sub>2</sub>O<sub>5</sub> as a function of magnetic field strength. Experimental spectra are shown in full lines, and best-fit simulations in black dashed lines. The simulations using site components are shown in red [site A (O1 and O3)] and blue [site B (O2)] dashed lines, based upon the experimental NMR parameters shown in Table 2. The green dashed line represents an O site that may be associated with partial hydration of the sample from contact with air. The asterisks denote the O signal arising from the ZrO<sub>2</sub> rotor.<sup>65</sup>

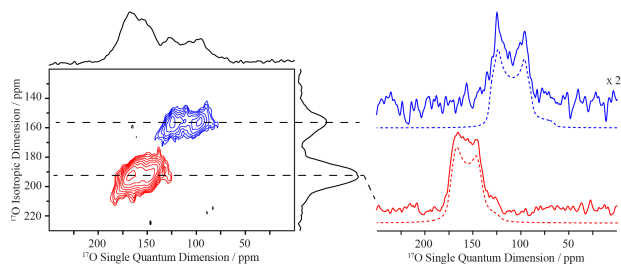


**Figure 4.** Two-dimensional  $^{17}\text{O}$  3QMAS spectrum of  $^{17}\text{O}$  enriched  $\text{Ba}_2\text{In}_2\text{O}_5$  obtained at 14.1 T. Right: experimental cross sections (full lines) obtained at  $\delta_1 = 156$  (blue) and 192 (red) ppm, along with best-fit simulations (dashed lines) using the experimental parameters given in Table 2.

This is also consistent with the nutation frequency behavior and with the absence of second-order quadrupolar broadening<sup>62</sup> observed previously. The  $^{17}\text{O}$  MAS NMR spectrum of  $^{17}\text{O}$  enriched  $\text{Ba}_2\text{In}_2\text{O}_4(\text{OH})_2$  obtained using a pulse length similar to the one measured by nutation on a water reference, reveals an intense and sharp resonance at 220 ppm (Figure S4). This will be further described in a forthcoming publication by the present authors.<sup>32</sup> Note also that no explicit pre-drying step prior to  $^{17}\text{O}$  enrichment was mentioned in the methodology of Adler *et al.*<sup>7</sup>

### 3.3. NMR GIPAW Calculations

It has been shown previously that differences in the chemical shifts and quadrupole parameters of  $^{17}\text{O}$  NMR in  $\text{ABO}_3$  metal-oxides depend strongly upon the B site cation species, the B-O bond distances, and the M–O–M (M=A or B cation) bond angles.<sup>46,66,67</sup> It is not obvious, however, whether the observed resonances can be unambiguously assigned and rationalized in light of these trends. Recent work on doped perovskites and other oxides,<sup>42,44,50</sup> demonstrate that  $^{17}\text{O}$  GIPAW NMR calculations are very reliable and likely to be of use in the present system also. The optimised structures obtained for  $\text{Ba}_2\text{In}_2\text{O}_5$  are used for a series of single point NMR calculations as described above. The computed  $^{17}\text{O}$  isotropic chemical shifts, anisotropies, asymmetries and quadrupole NMR parameters are fully detailed in the SI, where the  $\delta_{\text{iso}}$  values were obtained using the fitted reference parameters discussed above. A broad range of  $\delta_{\text{iso}}$  values emerge, as is evident in Figure 5a. Averaging over the shifts obtained in the ground and four near-degenerate perturbed structures (all within a range  $0.2 \text{ kJmol}^{-1}$  of the lowest energy structure) separately for each O sublattice leads to values of 181.6, 158.2 and 195.4 ppm in a 2:2:1 ratio for the O1, O2 and O3 sites, respectively, in the  $\cdots\text{OctTetOctTet}\cdots$  arrangement. The range in O2 values, at approximately 5.5 ppm, is larger than those obtained for the other two sites, and may be attributed to the broader range of In–O bond lengths experienced by the O2 sites (see Table 1). In particular, the optimisations reveal generally more asymmetric In–O2 bond lengths as compared with the O1 and O3 values and larger deviation from linearity in In–O2–In bond angles compared to In–O1–In in the  $\cdots\text{OctTetOctTet}\cdots$  arrangement (Table 1).

The computed oxygen Mulliken charges have also been examined, so as to discern any potential correlation with  $\delta_{\text{iso}}$

values, but it is found that the charges vary in only a narrow range from  $-0.94$  to  $-0.96 |e|$  across O sites. So, we instead turn to examine the distribution of In–O bond lengths and Mulliken overlap populations.

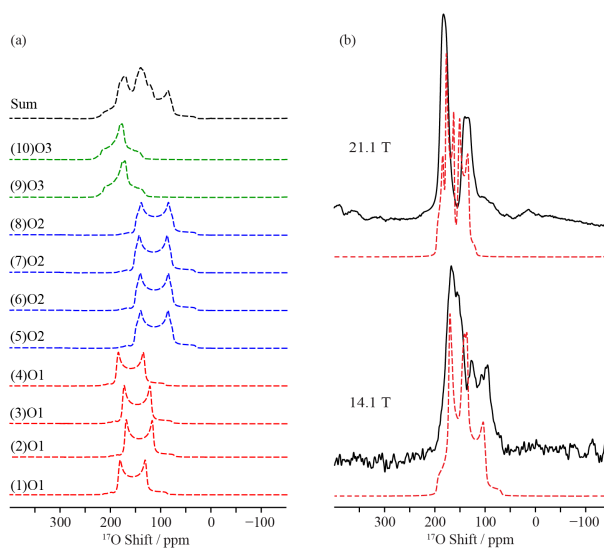


**Figure 5.** (a) Dashed black line: simulation of the GIPAW calculated  $^{17}\text{O}$  NMR spectra of the sum of all O sites of one (the lowest energy) of the five optimized  $\text{Ba}_2\text{In}_2\text{O}_5$  structures having the  $\cdots\text{OctTetOctTet}\cdots$  staggered arrangement. The  $\text{Ba}_2\text{In}_2\text{O}_5$  cell in  $P1$  symmetry generates 10 crystallographically distinct O sites, which are grouped into the O1, O2 and O3 sites, based on their labeling in the higher symmetry space groups (Figures 1 and 2). Color dashed lines: simulation of the GIPAW calculated  $^{17}\text{O}$  NMR spectra of the individual O sites (color grouped and noted for O1, O2 and O3 sublattices) of the same structure. All spectra were simulated at 14.1 T. (b) Comparison of the experimental  $^{17}\text{O}$  NMR spectra of  $\text{Ba}_2\text{In}_2\text{O}_5$  (solid black lines) and the sum of the simulated GIPAW calculated  $^{17}\text{O}$  NMR spectra (dashed red lines) for all five near-degenerate  $\text{Ba}_2\text{In}_2\text{O}_5$   $\cdots\text{OctTetOctTet}\cdots$  arrangements at magnetic field strengths of 14.1 and 21.1 T.

We find that the comparatively large shieldings of the O2 nuclei are associated with a strongly asymmetric bonding environment characterised by mean bond lengths of 2.064 and 2.364 Å, associated with mean Mulliken overlap populations of 0.50 and 0.26  $|e|$ , respectively. For comparison, the mean distances and overlap populations at O1 sites are 2.174 and 2.177 Å, and 0.34 and 0.34  $|e|$ , respectively; while, for O3 sites, the values are 2.111 and 2.122 Å, and 0.39 and 0.37  $|e|$ , respectively. On this basis, it is suggested that the high chemical shieldings of the O2 sites may be due to the heightened polarization of these anions. In support of this suggestion, we note the study by Bastow *et al.*<sup>66</sup> of a wide range of  $\text{ABO}_3$  and  $\text{A}_2\text{BO}_3$  phases, which found a strong correlation between the degree of anion polarization and the measured chemical shift. In the interest of completeness, the  $^{115}\text{In}$  and  $^{135/137}\text{Ba}$  NMR parameters are also calculated and presented in SI, although they are not experimentally measured here.

**Table 2. Experimental and calculated  $^{17}\text{O}$  isotropic chemical shift,  $\delta_{\text{iso}}$  (ppm); quadrupole coupling constant,  $C_Q$  (MHz); and quadrupole asymmetry  $\eta_Q$  for  $\text{Ba}_2\text{In}_2\text{O}_5$ . Standard deviations are also given for the calculated parameters; those for  $C_Q$  and  $\eta_Q$  values are less than 0.01 and so are omitted.**

Structure	Environment	$\delta_1$ (ppm) <sup>a</sup>	$\delta_{\text{iso}}$ (ppm)	$C_Q$ (MHz)	$\eta_Q$	$N^b$
Experimental <sup>c</sup>						
$\text{Ba}_2\text{In}_2\text{O}_5$	Site A (O1+O3)	192	179(4)/189(8) <sup>d</sup>	5.0(2)	0.2(1)	0.6
	Site B (O2)	156	138(4)/146(8) <sup>d</sup>	5.8(2)	0.2(1)	0.4
Calculated <sup>e</sup>						
···OctTetOctTet'···	O1	199.2 (sd 6.7)	181.6 (sd 4.2)	-5.74	0.05	0.4
	O2	179.2 (sd 4.9)	158.2 (sd 3.1)	-6.27	0.15	0.4
	O3	211.3 (sd 4.1)	195.4 (sd 2.6)	-4.70	0.89	0.2
···OctTetOctTet···	O1 <sub>a</sub>	221.3 (sd 2.7)	203.6 (sd 1.7)	-5.77	0.02	0.2
	O1 <sub>b</sub>	169.9 (sd 1.9)	152.1 (sd 1.2)	-5.73	0.09	0.2
	O2	178.6 (sd 4.3)	158.2 (sd 2.7)	-6.19	0.14	0.4
	O3	214.8 (sd 5.1)	198.4 (sd 3.2)	-4.57	0.98	0.2

<sup>a</sup> Slices were extracted from the isotropic dimension of the MQMAS spectrum at isotropic shifts of  $\delta_1$  (ppm). The calculated values of  $\delta_1$  are obtained with

$$\delta_1 = \frac{27\delta_{\text{iso}} - 10\delta_2}{17} \text{ with } \delta_2 = \delta_{\text{iso}} - \frac{3}{500} \frac{C_Q^2 \left(1 + \frac{\eta_Q^2}{3}\right)}{v_0^2} \text{ for } ^{17}\text{O} (I = 5/2) \text{ (see ref } ^{62}), \text{ the errors arising from the range of } \delta_{\text{iso}} \text{ values. } ^b \text{ Molar fraction of the site in the}$$

structure specified. <sup>c</sup> Obtained from the 3QMAS experiment and 1D spectra, and calculated as  $\delta_{\text{iso}} = \left(\frac{10}{27}\right)\delta_2 + \left(\frac{17}{27}\right)\delta_1$ . <sup>d</sup> The first listed  $\delta_{\text{iso}}$  value is obtained by a joint fit of the 1D and MQMAS spectra. The second value was obtained by analysing the field dependence of the 1D spectra. <sup>e</sup> Obtained from the averaged DFT calculated NMR parameters of the five perturbed and structurally re-optimized ground state structures (···OctTetOctTet'···) and the four perturbed and structurally re-optimized high-energy structures (···OctTetOctTet···).

On the basis of the  $^{17}\text{O}$  GIPAW calculations we assign the experimental  $^{17}\text{O}$  resonance at  $\delta_{\text{iso}} = 179$  ppm (Table 2) to a combination of the O1 and O3 sites, while the experimental site seen at  $\delta_{\text{iso}} = 138$  ppm is assigned to the O2 site (Figures 3a and 4). However, it is clear that the experimental splitting  $\delta(\text{O1+O3}) - \delta(\text{O2}) = 41$  ppm is underestimated by the calculations, which yield a value of 30 ppm. Note, however, that the mean absolute error in calculated  $^{17}\text{O}$  shifts arising from the shielding reference amounts to 12 ppm, as discussed above.<sup>50</sup> Figure 5b plots the comparison between the experimental and calculated  $^{17}\text{O}$  spectra at both 14.1 and 21.1 T (see Figure S3 for both the experimental and the computed  $^{17}\text{O}$  spectra at magnetic field strengths of 8.5, 11.7, 14.1 and 21.1 T) where the underestimated separation of peaks by the calculations is more clearly visible. The reason for this apparent discrepancy remains the subject of ongoing work.

The calculations provide  $C_Q$  values of the same order of magnitude for all three sites (Table 2), while the EFG asymmetry parameters,  $\eta_Q$ , vary more markedly, reaching a maximum for the tetrahedral sublattice. The difference between the mean of the computed O1 and O3  $C_Q$  value and the O2  $C_Q$  value, of approximately 1.0 ( $\pm 0.5$ ) MHz, is in very good agreement with the difference 0.8 ( $\pm 0.4$ ) MHz obtained from the fits to the experimental spectrum discussed above. The calculated O1  $C_Q$  value is approximately 15% larger than the experimental one extracted by assuming that the higher frequency resonance can be fit with one set of NMR parameters. In summary, the present first principles calculations provide a clear assignment of the experimental NMR data of  $\text{Ba}_2\text{In}_2\text{O}_5$ , although some discrepancies remain. We ascribe this to three main factors. The first error is ascribed to the errors inherent to the DFT method. Second errors between the calculated O1 NMR parameters and the experimental values result from the fitting of the lineshape of the major experimentally observed resonance with only a set of parameters, even though it must originate from multiple O1 (and O3) sites. Unfortunately, the lack of any further distinct features,

despite acquiring spectra at multiple fields, meant that a fit to the lineshape using more than one set of NMR parameters could not be justified. Third, it is not practical to sample all the possible (i.e., energetically favourable) configurations of this disordered structure within our DFT calculations. Some higher temperature configurations may also be trapped on cooling to room temperature, which may yield additional oxygen disorder that again we have not captured in our calculations. No evidence for any sites with a small  $C_Q$  values emerges from these calculations, confirming that the narrow resonance observed at 220 ppm in some of the experimental spectra is unlikely to arise from an O3 site in the dry material.

In order to explore whether the high-energy state ···OctTetOctTet··· structures contribute to the experimental NMR spectrum, we first note that the difference in formation energies of ground and excited arrangements is only 5 kJmol<sup>-1</sup> (per  $\text{Ba}_2\text{In}_2\text{O}_5$  formula unit). As a local region of ···OctTetOctTet··· O vacancy stacking can be created by moving just a few O ions, it is possible that regions of this structure could form due to thermal fluctuations or could be kinetically trapped in the lattice at lower temperatures. The calculated spectra of the lowest energy ···OctTetOctTet··· arrangement and the

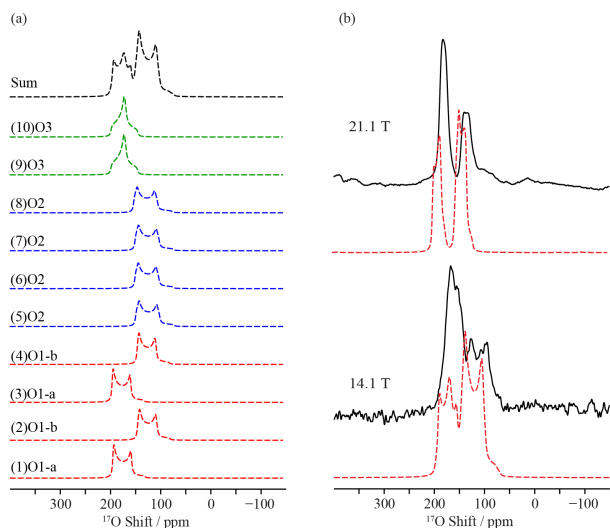


**Figure 6.** (a) Dashed black line: simulation of the GIPAW calculated  $^{17}\text{O}$  NMR spectra of the sum (scaled down by a factor 10) of all O sites of one (the lowest energy) of the four optimized  $\text{Ba}_2\text{In}_2\text{O}_5$  structures having the  $\cdots\text{OctTetOctTet}\cdots$ , stacked, arrangement. Color dashed lines: simulation of the GIPAW calculated  $^{17}\text{O}$  NMR spectra of the individual O sites (color grouped and noted for O1, O2 and O3 sublattices) of the same structure. All spectra were at 14.1 T. (b) Comparison of the experimental  $^{17}\text{O}$  NMR spectra of  $\text{Ba}_2\text{In}_2\text{O}_5$  (solid black lines) and the sum of the simulated of the GIPAW calculated  $^{17}\text{O}$  NMR spectra (dashed red lines) for all four  $\text{Ba}_2\text{In}_2\text{O}_5$ , near-degenerate  $\cdots\text{OctTetOctTet}\cdots$  arrangements at magnetic field strengths of 14.1 and 21.1 T.

decomposition into individual O sites is shown in Figure 6a. Interestingly, the O1 sites in this structure split into groups: the first, having somewhat higher chemical shifts than those in the  $\cdots\text{OctTetOctTet}\cdots$ , ground state, arrangement ( $\delta_{\text{iso}} = 203.6$  ppm, labelled O1<sub>a</sub> in Table 2); and the second, shifts somewhat lower than in the low energy arrangement and closer to the O2 values ( $\delta_{\text{iso}} = 152.1$  ppm, labelled O1<sub>b</sub> in Table 2). Thus, it is possible that there is a contribution from the high-energy state arrangement to the experimentally observed spectrum, and that it is likely to be difficult to resolve such a contribution. However, it cannot be significant, given that simulations of the spectrum of the high-energy state arrangement predict an intensity ratio for high and low frequency resonances of 2:3, which is not consistent with the experimentally observed intensity ratio.

## 4. Conclusions

In summary, this paper reports a comprehensive analysis of the Brownmillerite  $\text{Ba}_2\text{In}_2\text{O}_5$  structure using solid-state  $^{17}\text{O}$  NMR spectroscopy in combination with solid-state DFT calculations of configurational energetics and NMR parameters. A similar analysis of the corresponding  $\text{Ba}_2\text{In}_2\text{O}_4(\text{OH})_2$  hydrated form, of interest as a solid proton conductor, will be presented in a forthcoming paper. Two distinct O environments in a 3:2 ratio were observed by  $^{17}\text{O}$  MAS NMR in  $^{17}\text{O}$  enriched  $\text{Ba}_2\text{In}_2\text{O}_5$ : the more intense resonance at  $\delta_{\text{iso}} = 179$  ppm (at 21.1 T) is attributed to the combination of the O1 and O3 oxygen sublattices, while the weaker resonance at  $\delta_{\text{iso}} = 138$  ppm comprises the O2 sublattice alone. The assignment is based on GIPAW NMR calculations on both the ground  $\cdots\text{OctTetOctTet}\cdots$  and high-energy state  $\cdots\text{OctTetOctTet}\cdots$  O vacancy arrangements, which indicate that O1 and O3 sites have similar chemical shifts and

quadrupolar couplings, preventing their separate resolution even at a very high magnetic field strength of 21.1 T. Notably the bridging O1 and O2 sites have similar calculated quadrupolar asymmetry parameters  $\eta_Q = 0.05$  and 0.15, the smaller O1 value reflecting the more linear In-O-In bonding arrangement. By contrast,  $\eta_Q$  for the bent ( $127.6^\circ$ ) In-O3-In site is very different at 0.9. The MQMAS data reveals a small distribution of environments consistent with some disorder in this material, rendering the separation of the O3 and O1 sites more difficult. An analysis of the excited  $\cdots\text{OctTetOctTet}\cdots$  arrangement NMR parameters reveals an intensity ratio for the high and low frequency shifts that is not consistent with that observed experimentally, suggesting that it is not present in significant concentrations.

This new assignment contradicts the previous proposal by Adler *et al.* that the two dominant but very different  $^{17}\text{O}$  resonances arose due to the presence of  $\text{InO}_4$  tetrahedra and  $\text{InO}_6$  octahedra.<sup>7</sup> The sharp resonance at 220 ppm previously attributed to the O3 site in the same previous study<sup>7</sup> is much more intense for samples that have been exposed to moisture, and is therefore tentatively re-assigned as originating from surface water. The structural models investigated here do not reproduce the 220 ppm shift and further study is required to address this point.

## 5. Acknowledgements

We thank Dr. Andrew Illott (Stony Brook University, USA) for helpful discussions. This work was supported in part by grants DMR050612 and CHE0714183 from the National Science Foundation, by grant DESC0001284 from the Department of Energy, by an Advanced Fellowship from the EU-ERC (C.P.G.) and by the EPSRC (D.S.M.). F.B. thanks the EU Marie Curie actions FP7 for an International Incoming fellowship (grant no 275212). Research carried out in part at the Center for Functional Nanomaterials, Brookhaven National Laboratory, NY, USA, which is supported by the U.S. Department of Energy, Office of Basic Energy Sciences, under contract number DE-AC02-98CH10886.

## Notes and references

<sup>a</sup>Department of Chemistry, Stony Brook University, Stony Brook, NY 11794-3400, USA

<sup>b</sup>Department of Chemistry, University of Cambridge, Lensfield Road, Cambridge CB2 1EW, UK

<sup>c</sup>Department of Materials Science and Engineering, University of Wisconsin, Madison, WI 53706, USA

\*Author to whom correspondence should be addressed. E-mail: cpg27@cam.ac.uk

† Electronic Supplementary Information (ESI) available: [X-ray diffraction patterns (Figure S1), variable  $B_0$  field dependence of the  $^{17}\text{O}$  MAS NMR shift of the centre of gravity of the two  $^{17}\text{O}$  signals in  $\text{Ba}_2\text{In}_2\text{O}_5$  (Figure S2), comparison of the experimental  $^{17}\text{O}$  MAS NMR spectra of  $\text{Ba}_2\text{In}_2\text{O}_5$  and the simulation of the calculated  $^{17}\text{O}$  NMR parameters of computed  $\text{Ba}_2\text{In}_2\text{O}_5$  (Figure S3),  $^{17}\text{O}$  MAS NMR spectrum of  $^{17}\text{O}$  enriched  $\text{Ba}_2\text{In}_2\text{O}_4(\text{OH})_2$  (Figure S4), detail of all configurations considered (CIF), optimized structures and complete GIPAW NMR data. This material is available free of charge via the Internet at <https://pubs.acs.org>.]. See DOI: 10.1039/c3cp53642d

1. L. Malavasi, C. A. J. Fisher and M. S. Islam, *Chem. Soc. Rev.*, 2010, **39**, 4370-4387.

2. S. Adler, S. Russek, J. Reimer, M. Fendorf, A. Stacy, Q. Huang, A. Santoro, J. Lynn, J. Baltisberger and U. Werner, *Solid State Ionics*, 1994, **68**, 193-211.
3. P. M. Woodward, *Acta Crystallogr. B*, 1997, **53**, 44-66.
4. J. Goodenough, J. Ruiz-Diaz and Y. Zhen, *Solid State Ionics*, 1990, **44**, 21-31.
5. V. Jayaraman, A. Magrez, M. Caldes, O. Joubert, F. Taulelle, J. Rodriguezcarvajal, Y. Piffard and L. Brohan, *Solid State Ionics*, 2004, **170**, 25-32.
6. K. R. Kendall, C. Navas, J. K. Thomas and H.-C. zur Loye, *Solid State Ionics*, 1995, **82**, 215-223.
7. S. B. Adler, J. A. Reimer, J. Baltisberger and U. Werner, *J. Am. Chem. Soc.*, 1994, **116**, 675-681.
8. M. S. Islam, R. A. Davies, C. A. J. Fisher and A. V. Chadwick, *Solid State Ionics*, 2001, **145**, 333-338.
9. V. V. Kharton, F. M. B. Marques and A. Atkinson, *Solid State Ionics*, 2004, **174**, 135-149.
10. T. R. S. Prasanna and A. Navrotsky, *J. Mater. Res.*, 1993, **8**, 4.
11. C. E. Mohn, N. L. Allan, C. L. Freeman, P. Ravindran and S. Stølen, *J. Solid State Chem.*, 2005, **178**, 346-355.
12. M. Yoshinaga, T. Fumoto and T. Hashimoto, *J. Electrochem. Soc.*, 2005, **152**, A1221.
13. T. Hashimoto, *J. Electrochem. Soc.*, 2002, **149**, A1381-A1384.
14. A. Rolle, R.-N. Vannier, N. V. Giridharan and F. Abraham, *Solid State Ionics*, 2005, **176**, 2095-2103.
15. A. A. Colville and S. Geller, *Acta Crystallogr. B*, 1971, **27**, 2311-2315.
16. D. H. Gregory and M. T. Weller, *J. Solid State Chem.*, 1993, **107**, 134-148.
17. S. A. Speakman, J. W. Richardson, B. J. Mitchell and S. T. Misture, *Solid State Ionics*, 2002, **149**, 247-259.
18. P. Berastegui, S. Hull, F. J. Garcia-Garcia and S. G. Eriksson, *J. Solid State Chem.*, 2002, **164**, 119-130.
19. W. Fischer, G. Reck and T. Schober, *Solid State Ionics*, 1999, **116**, 211-215.
20. T. Hahn, *International tables for crystallography*, For International Union of Crystallography by Springer, Dordrecht, The Netherlands, 2005.
21. B. C. H. Steele, in *High Conductivity Solid Ionic Conductors: Recent Trends and Applications*, ed. T. Takahashi, World Scientific Publishing Co. Inc., Teaneck, NJ, 1989, p. 690.
22. K. T. Mueller, B. Q. Sun, G. C. Chingas, J. W. Zwanziger, T. Terao and A. Pines, *Journal of Magnetic Resonance (1969)*, 1990, **86**, 470-487.
23. E. F. Bertaut, P. Blum and A. Sagnières, *Acta Crystallogr.*, 1959, **12**, 149-159.
24. C. A. J. Fisher and M. S. Islam, *Solid State Ionics*, 1999, **118**, 355-363.
25. C. A. J. Fisher, M. S. Islam and R. J. Brook, *J. Solid State Chem.*, 1997, **128**, 137-141.
26. M. Kanzaki and A. Yamaji, *Mat. Sci. Eng. B-Solid*, 1996, **41**, 46-49.
27. J.-R. Martinez, C. E. Mohn, S. Stølen and N. L. Allan, *J. Solid State Chem.*, 2007, **180**, 3388-3392.
28. C. E. Mohn, N. L. Allan, C. L. Freeman, P. Ravindran and S. Stølen, *Phys. Chem. Chem. Phys.*, 2004, **6**, 3052.
29. Y.-L. Lee and D. Morgan, Ab Initio Study of Oxygen-Vacancy Ordering in Oxygen Conducting Ba<sub>2</sub>In<sub>2</sub>O<sub>5</sub>, MRS Proceedings, Armstrong, T., Masquelier, C., Sadaoka, Y., Traversa, E., Eds., 2006.
30. L. Frydman and J. S. Harwood, *J. Am. Chem. Soc.*, 1995, **117**, 5367-5368.
31. A. Medek, J. S. Harwood and L. Frydman, *J. Am. Chem. Soc.*, 1995, **117**, 12779-12787.
32. R. Dervişoğlu, D. S. Middlemiss, F. Blanc, L. A. Holmes, Y.-L. Lee, D. Morgan and C. P. Grey, *in preparation*.
33. C. Pickard and F. Mauri, *Phys. Rev. B*, 2001, **63**, 1-13.
34. T. Charpentier, *Solid State Nucl. Magn. Reson.*, 2011, **40**, 1-20.
35. C. Gervais, M. Profeta, F. Babonneau, C. J. Pickard and F. Mauri, *J. Phys. Chem. B*, 2004, **108**, 13249-13253.
36. A. Wong, G. Thurgood, R. Dupree and M. E. Smith, *Chem. Phys.*, 2007, **337**, 144-150.
37. E. Salager, G. M. Day, R. S. Stein, C. J. Pickard, B. Elena and L. Emsley, *J. Am. Chem. Soc.*, 2010, **132**, 2564-2566.
38. S. E. Ashbrook, A. J. Berry, D. J. Frost, A. Gregorovic, C. J. Pickard, J. E. Readman and S. Wimperis, *J. Am. Chem. Soc.*, 2007, **129**, 13213-13224.
39. S. E. Ashbrook, L. Le Polles, G. Regis, C. J. Pickard and R. I. Walton, *Phys. Chem. Chem. Phys.*, 2006, **8**, 3423-3431.
40. K. E. Johnston, J. M. Griffin, R. I. Walton, D. M. Dawson, P. Lightfoot and S. E. Ashbrook, *Phys. Chem. Chem. Phys.*, 2011, **13**, 7565-7576.
41. K. E. Johnston, C. C. Tang, J. E. Parker, K. S. Knight, P. Lightfoot and S. E. Ashbrook, *J. Am. Chem. Soc.*, 2010, **132**, 8732-8746.
42. F. Blanc, D. S. Middlemiss, Z. Gan and C. P. Grey, *J. Am. Chem. Soc.*, 2011, **133**, 17662-17672.
43. F. Blanc, D. S. Middlemiss, L. Buannic, J. L. Palumbo, I. Farnan and C. P. Grey, *Solid State Nucl. Magn. Reson.*, 2012, **42**, 87-97.
44. L. Buannic, F. Blanc, D. S. Middlemiss and C. P. Grey, *J. Am. Chem. Soc.*, 2012, **134**, 14483-14498.
45. A. R. West, *Solid state chemistry and its applications*, Wiley, Chichester, 1984.
46. S. E. Ashbrook and M. E. Smith, *Chem. Soc. Rev.*, 2006, **35**, 718-735.
47. J.-P. Amoureux, C. Fernandez and S. Steuernagel, *J. Magn. Reson.*, 1996, **Series A 1**, 116-118.
48. BRUKER, *Topspin 3.1, software for NMR spectral analysis*, Bruker Biospin, Rheinstetten, Germany, 2011.
49. J. D. van Beek, *J. Magn. Reson.*, 2007, **187**, 19-26.
50. D. S. Middlemiss, F. Blanc, C. J. Pickard and C. P. Grey, *J. Magn. Reson.*, 2010, **204**, 1-10.
51. N. S. Barrow, J. R. Yates, S. A. Feller, D. Holland, S. E. Ashbrook, P. Hodgkinson and S. P. Brown, *Phys. Chem. Chem. Phys.*, 2011, **13**, 5778-5789.
52. S. W. Reader, M. R. Mitchell, K. E. Johnston, C. J. Pickard, K. R. Whittle and S. E. Ashbrook, *J. Phys. Chem. C*, 2009, **113**, 18874-18883.
53. M. R. Mitchell, S. W. Reader, K. E. Johnston, C. J. Pickard, K. R. Whittle and S. E. Ashbrook, *Phys. Chem. Chem. Phys.*, 2011, **13**, 488-497.
54. S. J. Clark, M. D. Segall, C. J. Pickard, P. J. Hasnip, M. I. J. Probert, K. Refson and M. C. Payne, *Z. Kristallogr.*, 2005, **220**, 567-570.
55. J. P. Perdew, K. Burke and M. Ernzerhof, *Phys. Rev. Lett.*, 1996, **77**, 3865-3868.
56. R. S. Mulliken, *J. Chem. Phys.*, 1955, **23**, 1833-1840.

- 
57. D. Sánchez-Portal, E. Artacho and J. M. Soler, *J. Phys.: Condens. Matter*, 1996, **8**, 3859.
  58. J. R. Yates, C. J. Pickard and F. Mauri, *Phys. Rev. B*, 2007, **76**, 024401.
  59. M. Profeta, F. Mauri and C. J. Pickard, *J. Am. Chem. Soc.*, 2003, **125**, 541-548.
  60. P. Pyykkö, *Mol. Phys.*, 2008, **106**, 1965-1974.
  61. M. Bak, J. T. Rasmussen and N. C. Nielsen, *J. Magn. Reson.*, 2000, **147**, 296-330.
  62. M. E. Smith and E. R. H. van Eck, *Prog. Nucl. Magn. Reson. Spectrosc.*, 1999, **34**, 159-201.
  63. D. Massiot, F. Fayon, M. Capron, I. King, S. Le Calvé, B. Alonso, J.-O. Durand, B. Bujoli, Z. Gan and G. Hoatson, *Magn. Reson. Chem.*, 2002, **40**, 70-76.
  64. G. L. Turner, S. E. Chung and E. Oldfield, *J. Magn. Reson.*, 1985, **64**, 316-324.
  65. K. J. D. MacKenzie and M. E. Smith, *Multinuclear Solid State NMR of Inorganic Materials*, Pergamon Press, 2002.
  66. T. J. Bastow, P. J. Dirken, M. E. Smith and H. J. Whitfield, *J. Phys. Chem.*, 1996, **100**, 18539-18545.
  67. J. L. Palumbo, T. A. Schaedler, L. Peng, C. G. Levi and C. P. Grey, *J. Solid State Chem.*, 2007, **180**, 2175-2185.